



Mechanism of Na⁺/H⁺ Antiporting

Isaiah T. Arkin, *et al.*

Science **317**, 799 (2007);

DOI: 10.1126/science.1142824

The following resources related to this article are available online at www.sciencemag.org (this information is current as of August 9, 2007):

Updated information and services, including high-resolution figures, can be found in the online version of this article at:

<http://www.sciencemag.org/cgi/content/full/317/5839/799>

Supporting Online Material can be found at:

<http://www.sciencemag.org/cgi/content/full/317/5839/799/DC1>

This article **cites 26 articles**, 11 of which can be accessed for free:

<http://www.sciencemag.org/cgi/content/full/317/5839/799#otherarticles>

This article appears in the following **subject collections**:

Biochemistry

<http://www.sciencemag.org/cgi/collection/biochem>

Information about obtaining **reprints** of this article or about obtaining **permission to reproduce this article** in whole or in part can be found at:

<http://www.sciencemag.org/about/permissions.dtl>

The DePreSys hindcast starting from June 1995 correctly predicted an initial cooling, followed by a general warming. As expected, the NoAssim hindcasts predicted only the general warming trend, although the NoAssim hindcast from June 1995 is generally too warm. In the DePreSys forecast, internal variability offsets the effects of anthropogenic forcing in the first few years, leading to no net warming before 2008 (Fig. 4). In contrast, the NoAssim forecast warms during this period. Regional assessment to February 2007 (fig. S8) indicates that this initial cooling in DePreSys relative to NoAssim results from the development of cooler anomalies in the tropical Pacific and the persistence of neutral conditions in the Southern Ocean. In both cases, the DePreSys forecast is closer to the verifying changes observed since the forecast start date. Both NoAssim and DePreSys, however, predict further warming during the coming decade, with the year 2014 predicted to be $0.30^{\circ} \pm 0.21^{\circ}\text{C}$ [5 to 95% confidence interval (CI)] warmer than the observed value for 2004. Furthermore, at least half of the years after 2009 are predicted to be warmer than 1998, the warmest year currently on record.

References and Notes

- S. Solomon *et al.*, Eds., *Climate Change 2007: The Physical Science Basis. Contribution of Working Group I to the Fourth Assessment Report of the Intergovernmental Panel on Climate Change* (Cambridge Univ. Press, Cambridge, 2007).
- M. Collins, M. R. Allen, *J. Clim.* **15**, 3104 (2002).
- P. A. Stott *et al.*, *Science* **290**, 2133 (2000).
- U. Cubasch *et al.*, in *Climate Change 2001: The Scientific Basis. Contribution of Working Group I to the Third Assessment Report of the Intergovernmental Panel on Climate Change*, J. T. Houghton *et al.*, Eds. (Cambridge Univ. Press, Cambridge, 2001), pp. 525–582.
- G. A. Meehl *et al.*, in *Climate Change 2007: The Physical Science Basis. Contribution of Working Group I to the Fourth Assessment Report of the Intergovernmental Panel on Climate Change*, S. Solomon *et al.*, Eds. (Cambridge Univ. Press, 2007), pp. 747–845.
- S. M. Griffies, K. Bryan, *Science* **275**, 181 (1997).
- A. Grötzer, M. Latif, A. Timmermann, R. Voss, *J. Clim.* **12**, 2607 (1999).
- M. Collins, B. Sinha, *Geophys. Res. Lett.* **30**, 1306 (2003).
- M. Latif *et al.*, *J. Clim.* **17**, 1605 (2004).
- H. Pohlmann *et al.*, *J. Clim.* **17**, 4463 (2004).
- G. J. Boer, *Clim. Dyn.* **23**, 29 (2004).
- S. B. Power, R. Colman, X. Wang, P. Hope, *Predictions in Ungauged Basins: International Perspectives on the State of the Art and Pathways Forward*, M. Franks, K. Sivapalan, K. Takeuchi, Y. Tachikawa, Eds. (Publication 301, International Association of Hydrological Science, Wallingford, UK, 2005).
- T. N. Palmer *et al.*, *Bull. Am. Meteorol. Soc.* **85**, 853 (2004).
- F. W. Zwiers, *Nature* **416**, 690 (2002).
- T. C. K. Lee, F. W. Zwiers, X. Zhang, M. Tsao, *J. Clim.* **19**, 5305 (2006).
- P. A. Stott, J. A. Kettleborough, *Nature* **416**, 723 (2002).
- C. Gordon *et al.*, *Clim. Dyn.* **16**, 147 (2000).
- Materials and methods are available as supporting material on Science Online.
- T. C. Johns *et al.*, *Clim. Dyn.* **20**, 583 (2003).
- Solar irradiance is projected by repeating the previous 11-year solar cycle. Volcanic aerosol is projected as an exponential decay with an e -folding time scale of 1 year. Our hindcasts therefore do not use solar or volcanic information that would not have been available at the time.
- We use the term “hindcast” to refer to a forecast made retrospectively using only data that would have been available at the time.

- Our hindcast period ends in 2001 because our hindcasts are initialized using the 40-year ECMWF (European Centre for Medium-Range Weather Forecasts) atmosphere reanalysis (18), the last complete year of which is 2001.
- The ensemble size for both DePreSys and NoAssim was further increased by combining with hindcasts from previous seasons. For hindcasts of the coming year, we combine two seasons, giving eight ensemble members. For longer lead times, we combine four seasons, giving 16 ensemble members.
- $\text{RMSE} = \sqrt{[\sum_{i=1}^N \bar{e}_i^2]/N}$ where N is the number of hindcasts and \bar{e}_i is the error of the ensemble mean for each hindcast i averaged over the required spatial region.
- DePreSys is designed to avoid trends during forecasts caused by systematic model errors. This is achieved by assimilating observed anomalies added to the model climatology and removing the model climatology to produce forecast anomalies. The climatological period is 1979–2001 for the atmosphere and 1941–1996 for the ocean. Further details are given in (18).
- A. J. Simmons, A. Hollingsworth, *Q. J. R. Meteorol. Soc.* **128**, 647 (2002).
- The confidence interval shown by the red shading in Figs. 2 and 4 should not be confused with the significance limits shown by the blue shading in Fig. 1. The confidence interval is a measure of the uncertainty in a forecast at a single time. The significance limits measure the uncertainty in differences between the skill of NoAssim and DePreSys averaged over all hindcasts.
- D. E. Parker, H. Wilson, P. D. Jones, J. R. Christy, C. K. Folland, *Int. J. Climatol.* **16**, 487 (1996).
- G. R. Harris *et al.*, *Clim. Dyn.* **27**, 357 (2006).
- We computed the RMSE of the linear trend in global T_e during the first 5 years of each hindcast. The RMSE values are 0.030 and 0.038°C per year for DePreSys and

NoAssim respectively, with the difference being significant at the 5% level.

- S. Levitus, J. Antonov, T. Boyer, *Geophys. Res. Lett.* **32**, L02604 (2005).
- S. Wilson, *Oceanus* **42**, 17 (2000).
- Model errors, such as those arising from uncertainties in climate change feedbacks (35), are liable to cause biases in predicted changes. We found a modest time-dependent bias in DePreSys hindcasts, unaffected by major volcanic eruptions, rising to $0.07^{\circ} \pm 0.02^{\circ}\text{C}$ for year 9 (fig. S6) and removed this from both DePreSys and NoAssim forecasts (Fig. 4).
- We issue the caveat that any major volcanic eruptions occurring during the forecast period would cool global T_e as compared to our forecast.
- B. J. Soden, I. M. Held, *J. Clim.* **19**, 3354 (2006).
- C. K. Folland *et al.*, *Geophys. Res. Lett.* **28**, 2621 (2001).
- D. E. Parker, L. V. Alexander, J. Kennedy, *Weather* **59**, 145 (2004).
- P. D. Jones, A. Moberg, *J. Clim.* **16**, 206 (2003).
- D. M. Smith, J. M. Murphy, *J. Geophys. Res.* **112**, C02022 (2007).
- We thank many colleagues in the Met Office for developing the climate models and for help and advice during the course of this work. This work was supported by the UK Department of the Environment, Food and Rural Affairs, and by the UK Government Meteorological Research Programme.

Supporting Online Material

www.sciencemag.org/cgi/content/full/317/5839/796/DC1
Materials and Methods
SOM Text
Figs. S1 to S8
References

4 January 2007; accepted 19 June 2007
10.1126/science.1139540

Mechanism of Na^+/H^+ Antiporting

Isaiah T. Arkin,^{1*} Huafeng Xu,¹ Morten Ø. Jensen,¹ Eyal Arbely,² Estelle R. Bennett,² Kevin J. Bowers,¹ Edmond Chow,¹ Ron O. Dror,¹ Michael P. Eastwood,¹ Ravenna Flitman-Tene,² Brent A. Gregersen,¹ John L. Klepeis,¹ István Kolossyváry,¹ Yibing Shan,¹ David E. Shaw^{1,3,†}

Na^+/H^+ antiporters are central to cellular salt and pH homeostasis. The structure of *Escherichia coli* NhaA was recently determined, but its mechanisms of transport and pH regulation remain elusive. We performed molecular dynamics simulations of NhaA that, with existing experimental data, enabled us to propose an atomically detailed model of antiporter function. Three conserved aspartates are key to our proposed mechanism: Asp¹⁶⁴ (D164) is the Na^+ -binding site, D163 controls the alternating accessibility of this binding site to the cytoplasm or periplasm, and D133 is crucial for pH regulation. Consistent with experimental stoichiometry, two protons are required to transport a single Na^+ ion: D163 protonates to reveal the Na^+ -binding site to the periplasm, and subsequent protonation of D164 releases Na^+ . Additional mutagenesis experiments further validated the model.

NhaA is the archetypal Na^+/H^+ antiporter and the only member of the family that is absolutely required by *E. coli* for survival in high-salt conditions, under alkaline stress, or in the presence of otherwise toxic Li^+ concentrations (1, 2). It is a membrane protein consisting

of 388 residues that traverse the inner membrane 12 times, with both termini ending in the cytoplasm (3). The structure of NhaA exhibits a distinctive fold of 10 contiguous transmembrane helices and 2 antiparallel, discontinuous helices (*iv* and *xi*) aligned end to end to span the membrane (4).

NhaA excretes Na^+ or Li^+ (but not K^+) from the cytoplasm using the energy from the cotransport of protons down their electrochemical gradient into the cell, with a characteristic electrogenic stoichiometry of two protons to one Na^+ or Li^+ (5, 6). NhaA's activity decreases by three orders of magnitude when shifting from pH 8 to pH 6.5 (7), enabling it to regulate cellular acidity in addition to cellular salinity.

¹D. E. Shaw Research, New York, NY 10036, USA. ²The Hebrew University of Jerusalem, Department of Biological Chemistry, Jerusalem 91904, Israel. ³Center for Computational Biology and Bioinformatics, Columbia University, New York, NY 10032, USA.

*On sabbatical leave from The Hebrew University of Jerusalem, Department of Biological Chemistry, Jerusalem, 91904, Israel.

†To whom correspondence should be addressed. E-mail: david@deshaw.com

Using recently developed algorithms for the high-speed, parallel execution of molecular dynamics (MD) simulations (8–11), we performed simulations of membrane-embedded NhaA with an aggregate length approaching 3 μs , allowing us to examine ion transport, pH regulation, and cation selectivity and to thereby deduce a detailed mechanistic picture of the function of NhaA.

Crystallization of *E. coli* NhaA was performed at pH 4, a state in which the protein is inactive, and accordingly, no Na^+ was seen in the structure (4). Hunte *et al.* (4) inferred, however, that the Na^+ -binding site is near D163 or D164 (12), because these have been shown to be the only carboxylic residues absolutely indispensable for transport activity (13). Because these residues are likely candidates to undergo protonation state changes that drive Na^+ transport, we simulated NhaA under all four possible combinations of the protonation states of D163 and D164. After equilibration, we initiated MD simulations (12 to 100 ns each) from each of these four configurations, with Na^+ placed adjacent to D163. We then repeated the process, placing Na^+ adjacent to D164.

When Na^+ was placed adjacent to D163, irrespective of the protonation state of D163 or D164, the ion became trapped by the protein, and water was unable to penetrate the protein to hydrate it; this finding suggests that D163 is not the Na^+ -binding site. The behavior of Na^+ was entirely different when placed adjacent to D164. If D164 was deprotonated, Na^+ remained bound regardless of the protonation state of D163, with water able to reach and hydrate the ion. Placing Na^+ adjacent to protonated D164, however, provided the strongest clues as to how the transporter might function. In this case, the ion was expelled from the protein to the aqueous environment, with the direction of Na^+ release determined by the protonation state of D163. If D163 was protonated, Na^+ was expelled to the periplasm; in contrast, if D163 was deprotonated, Na^+ was expelled to the cytoplasm. (See Fig. 1A.)

We therefore propose that D163 and D164 play different roles in the Na^+ transport mechanism. D164 is the binding site for Na^+ : Its protonation state determines whether the Na^+ binds to the protein or is released. When D164 is deprotonated and, consequently, negatively charged, Na^+ remains tightly bound as a result of Coulombic attraction. When D164 is protonated, the electrostatic interaction is diminished and Na^+ no longer binds. In contrast, D163 is the accessibility-control site of the protein: Its protonation state is the molecular switch that determines whether the Na^+ -binding site (i.e., D164) is accessible to the periplasm or to the cytoplasm. Bound Na^+ can be expelled to the periplasm if D163 is protonated or to the cytoplasm if D163 is deprotonated; in each case, expulsion is accompanied by protonation of D164.

Our simulations provide a structural explanation for how D163 acts as a conformational switch. The carboxylate group of deprotonated D163 makes strong hydrogen bonds with the

amide hydrogens of residues M105 and T132 (Fig. 2). Upon protonation, these interactions vanish, and D163 forms a new hydrogen bond between its carboxylic hydrogen and the carbonyl oxygen of M105. This movement causes helix ν to tilt, which shifts the Na^+ -binding site (D164) in the direction of the periplasm.

The local structural changes elicited by D163 protonation lead to global conformational

changes (Fig. 2). When D163 is protonated, the cytoplasmic entrance is closed while the periplasmic exit is open. Deprotonation of D163 leads to the closure of the periplasmic Na^+ exit and the opening of the cytoplasmic entrance. Taken together, our data provide a molecular realization of the alternate accessibility mechanism postulated by Jardetzky more than 40 years ago (14).

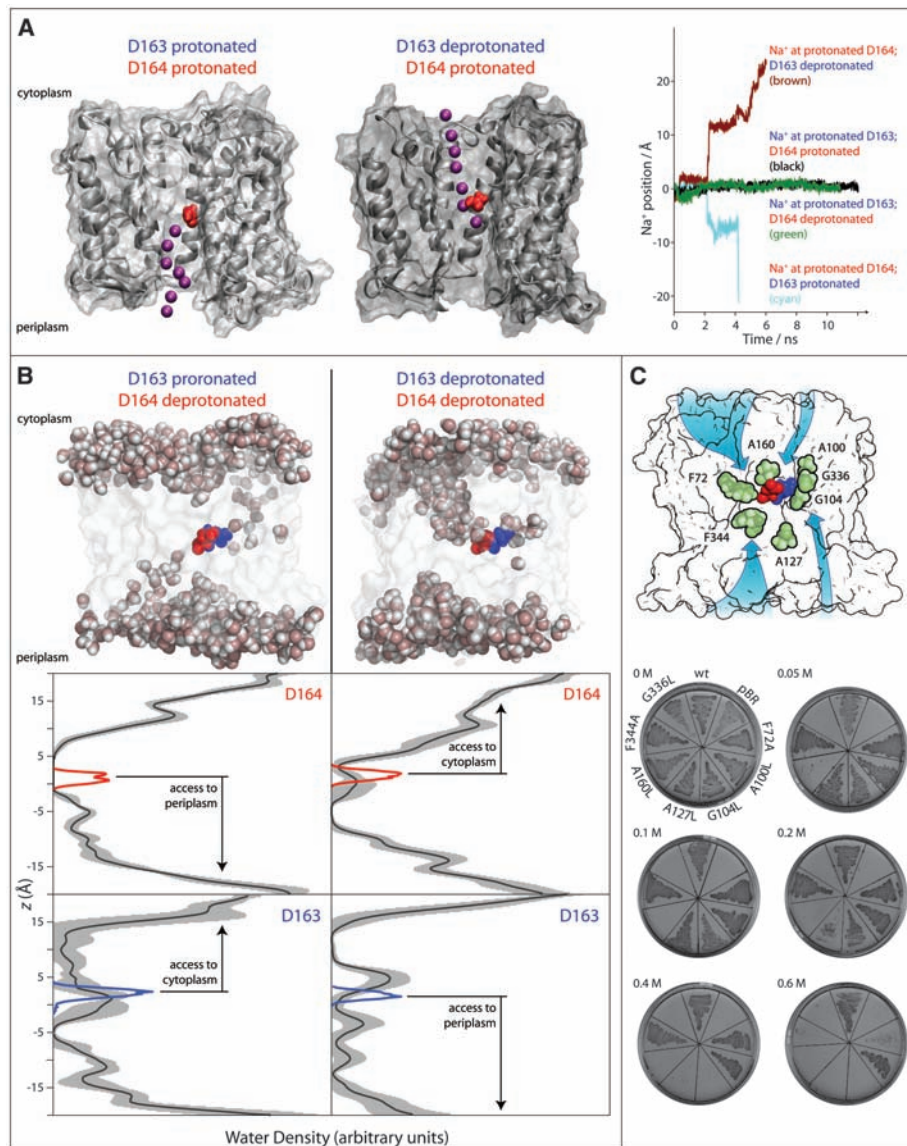


Fig. 1. Na^+ transport and alternating access. D163 and D164 are colored in blue and red, respectively. (A) Series of Na^+ (purple) positions when D163 (not shown) is deprotonated or protonated, leading to Na^+ expulsion to the cytoplasm or transport to the periplasm, respectively. The rightmost panel depicts Na^+ position as a function of time in different D163 and D164 protonation states. (B) The four graphs show water penetration into the occupied Na^+ -binding site at D164 (top graphs) and the regulatory site at D163 (bottom graphs) as a function of position (z) across the membrane. The average density and SD were computed from two 60-ns trajectories, with D163 protonated (left) and deprotonated (right). Blue and red lines in graphs represent positions of D163 and D164, respectively. The top panel shows representative snapshots from the simulations, with water molecules shown in pink and white. (C) Mutagenesis studies of NhaA. Wild-type (WT) and mutated antiporters were assayed at different NaCl concentrations. Negative control bacteria (pBR) expressed no antiporter. The top panel shows locations of the different mutation sites (green) in the NhaA structure. Substrate pathways from the cytoplasm and periplasm are indicated by blue arrows. Molecular images in Figs. 1, 2, and 4 and Fig. S1 were produced by VMD (29), and Fig. 1 and Fig. S3 were generated by PyMOL (30).

The hypothesis that the protein contains a Na^+/H^+ -binding site at D164 and a H^+ -binding site at D163 implies that protons and Na^+ must be able to reach D164 and that protons must be able to reach D163. A putative Na^+ transport pathway, notably blocked in the inactivated x-ray structure, has been suggested (4), starting from a large crevice on the cytoplasmic face of the protein, leading to D164, and ending in the periplasm. However, the existence of a pathway to D163 has not been previously considered.

To identify possible ion transport pathways, we determined the water accessibility of the two sites for different protonation states of the protein. Water can reach both D163 and D164 from both sides of the membrane (Fig. 1B), but in no pro-

tonation state is there a continuous water density across the protein; such water connectivity might deplete the proton motive force. Instead, when D163 is accessible to the cytoplasm, D164 is accessible to the periplasm (Fig. 1B, left panels), and when D163 is accessible to the periplasm, D164 is accessible to the cytoplasm (Fig. 1B, right panels).

We undertook mutagenesis experiments to substantiate our computational finding of these water pathways to D163. We hypothesized that replacing smaller amino acids with larger ones along these pathways would block access of protons to D163 and thus inhibit the antiporter. Activities of wild-type and mutant antiporters were assayed for their ability to sustain growth

of bacteria that do not harbor any of the three native antiporter genes (15). Unlike the wild-type antiporters, all mutant antiporters aside from $\text{Ala}^{100} \rightarrow \text{Leu}^{100}$ (A100L) failed to support growth in elevated concentrations of NaCl (Fig. 1C). Because the G336L mutant protein does not support bacterial growth even in a low concentration of NaCl , it is possible that this protein may be unstable and nonfunctional. The functional comparisons between the mutant antiporters were conducted *in vivo*, and the concentrations of the different proteins may thus differ despite identical handling.

The inhibitory effects of mutations at A127 and G104 are consistent with blockage of a water-mediated proton pathway to D163 from the periplasm, whereas the inhibitory effect of a mutation of A160 is consistent with blockage of a water-mediated proton entry to D163 from the cytoplasm. Moreover, we explicitly simulated the effect of mutating A127 to leucine (fig. S3) and found that water and, therefore, proton penetration from the periplasm to D163 are indeed blocked. Additional mutagenesis results are reported in the supporting online material (SOM).

Based on these results, we propose a mechanism for the Na^+/H^+ antiporting cycle of NhaA that consists of the following four sequential steps (labeled as in Fig. 3): (A) The accessibility-control site (D163) is deprotonated, resulting in cytoplasmic accessibility of the Na^+ -binding site. The Na^+ -binding site (D164) therefore releases a H^+ to, and takes up a Na^+ from, the cytoplasm. (B) The accessibility-control site (D163) is protonated by a H^+ that enters from the periplasm. This results in a conformational change (Fig. 2) that exposes the Na^+ -binding site to the periplasm. (C) The Na^+ -binding site (D164) exchanges the bound Na^+ with a H^+

Fig. 2. Effects of D163 protonation state on antiporter conformation. D164 is protonated, such that bound Na^+ would be expelled. The top panels depict the local interaction of D163, whereas the bottom panels illustrate the global conformation of the protein. The structures in which D163 is protonated (orange) and deprotonated (white) are superposed by C_α atoms (D164 is protonated in both structures). The C_α root mean square deviation (RMSD) between the structures is ~ 2.3 Å when comparing the central helices *ii* to *v*, *ix*, and *xi*.

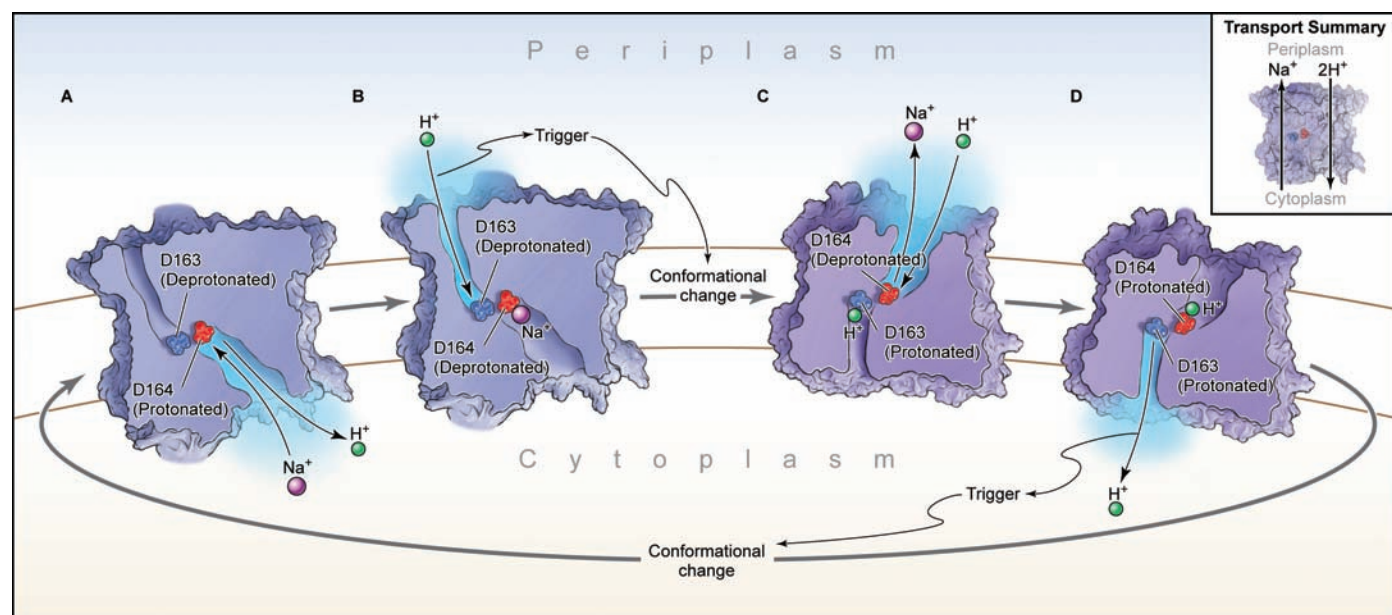
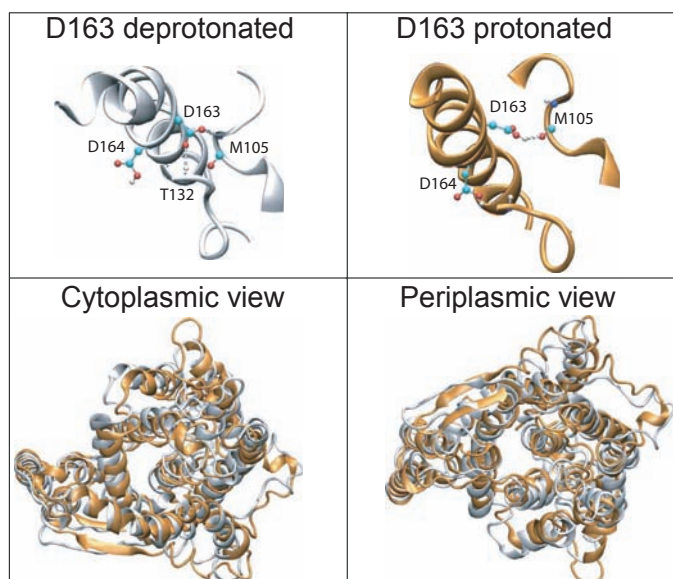
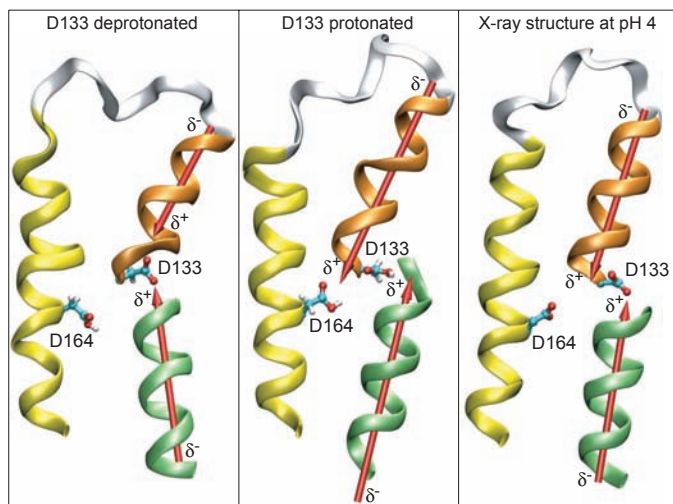


Fig. 3. Schematic representation of the transport model of NhaA. The carboxylic group of D163 in the accessibility-control site is colored blue, and D164 in the Na^+ -binding site is red.

from the periplasm. The replacement of bound Na^+ by H^+ could be considered a “knock-on”-like mechanism (16) acting through electrostatic repulsion (17). (D) D163 deprotonates, leading to a protein conformational change that again exposes the Na^+ -binding site (D164) to the cytoplasm. Overall, two protons are taken up from the periplasm in panels B and C and released to the cytoplasm in panels A and D (Fig. 3), while a single Na^+ is taken up from the cytoplasm in panel A and then pumped to the periplasm in panel C, which is consistent with NhaA's electrogenic stoichiometry of one Na^+ to two protons (5).

Very recent simulations of NhaA (18) have explored conformational changes associated with the simultaneous deprotonation of a group of residues (not including D133, discussed below), but a detailed understanding of the mechanism of its pH sensitivity and the identity of its pH sensor has remained elusive. Although the pH activation range of NhaA closely resembles the pK_a of histidine (where K_a is the acid dissociation constant), no single histidine is required for Na^+ transport or is part of the pH sensor (19, 20). We thus focused instead on carboxylic residues as possible pH sensors, because some carboxylic residues are known to have highly elevated pK_a 's (21, 22). Recently, pK_a 's of all ionizable residues were calculated for acid-inactivated NhaA (23). Six carboxylic residues (D78, E82, E124, D133, D163, and D164) were found to have abnormally high pK_a 's, with D133 having the highest value. Having already conducted simulations with protonated D163 and D164, we performed four additional simulations (6 ns each): In each of these additional simulations, either D78, E82, E124, or D133 was protonated (with D163 and D164 protonated in all cases). Protonating the “real” pH sensor should lead the protein to adopt a structure similar to the x-ray structure, which was determined at low pH (4), conditions under which the pH sensor is presumably protonated.

Fig. 4. Effect of D133 protonation on NhaA structure. The leftmost and middle panels display the structures resulting from simulations in which D133 was deprotonated or protonated. The rightmost panel displays the x-ray crystal structure obtained at pH 4 (4). Due to the resolution of the x-ray analysis (3.45 Å), no hydrogen is seen in the structure. Red arrows highlight the positions of the helical axes. The helix coloring is as described in fig. S1. The change from the x-ray structure in a simulation with D133 protonated is noticeably smaller than the corresponding change when D133 is deprotonated ($C\alpha$ RMSD of 2.0 Å versus 2.5 Å when comparing helices *ii*, *iv*, *v*, and *xi*).



Our simulations suggest that D133 is a key component of the pH sensor. D133 resides between the N termini of helix *iv* and helix *xi*, thereby neutralizing their opposing helical dipoles (Fig. 4). Upon protonation of D133, the two opposing helices shift such that their dipoles no longer converge on a single point, because a protonated carboxylic group cannot effectively neutralize the opposing dipoles. This conformation is similar to the acid-inactivated x-ray structure (4). Moreover, among those carboxylic residues exhibiting elevated pK_a 's (23), D133 was the only one whose protonation resulted in such a conformational change.

Mechanistically, the shift of the two helical dipoles observed in our simulations upon D133 protonation causes D164 in the Na^+ -binding site to face the protein lumen rather than the Na^+ entry and exit pathways (Fig. 4). In this position, D164 is unable to bind Na^+ , resulting in an inactive protein. D164 also faces the protein lumen in the low-pH x-ray structure, further pointing to D133 as the pH sensor. Mutation of D133 to the neutral residue asparagine has been shown experimentally (13, 24) to result in nearly complete inhibition of transport, similar to the inactivation caused by lowering of pH. Moreover, mutation of G338, located at the juncture between the helical dipoles, markedly reduces the pH response of the transporter (25).

The antiporter must be, and is (6), extremely selective for Na^+ over K^+ , and is slightly selective for Li^+ over Na^+ (26, 27). To investigate NhaA's selectivity among different cations, we conducted free-energy perturbation calculations (28) and found that NhaA (i) binds Li^+ more strongly than Na^+ (by 16 kJ/mol) and (ii) binds K^+ more weakly than Na^+ (by 14 kJ/mol) (fig. S4A). Potential of mean force analyses (28) show that neither Na^+ nor Li^+ encounters a substantial kinetic barrier to binding (fig. S4B). Our results indicate that NhaA's ion selectivity can be explained thermodynamically.

Our combinatorial approach, based on multiple long-time-scale MD simulations, led to the formulation of a model of NhaA's transport mechanism, pH regulation, and cation selectivity that is consistent with both our own and previously reported experimental data. Future studies will be needed to (i) identify the exact source of coupling between Na^+ and proton transport, which is necessary to avoid proton leakage by NhaA, and (ii) determine whether mammalian Na^+/H^+ exchangers, which differ in their $\text{Na}^+:\text{H}^+$ stoichiometry and pH response, use a transport mechanism similar to that proposed for NhaA.

References and Notes

- E. Padan, M. Venturì, Y. Gerchman, N. Dover, *Biochim. Biophys. Acta* **1505**, 144 (2001).
- E. Padan *et al.*, *Biochim. Biophys. Acta* **1658**, 2 (2004).
- A. Rothman, E. Padan, S. Schuldiner, *J. Biol. Chem.* **271**, 32288 (1996).
- C. Hunte *et al.*, *Nature* **435**, 1197 (2005).
- D. Taglicht, E. Padan, S. Schuldiner, *J. Biol. Chem.* **268**, 5382 (1993).
- S. Schuldiner, H. Fishkes, *Biochemistry* **17**, 706 (1978).
- D. Taglicht, E. Padan, S. Schuldiner, *J. Biol. Chem.* **266**, 11289 (1991).
- D. E. Shaw, *J. Comput. Chem.* **26**, 1318 (2005).
- K. J. Bowers, R. O. Dror, D. E. Shaw, *J. Comput. Phys.* **221**, 303 (2007).
- K. J. Bowers, R. O. Dror, D. E. Shaw, *J. Chem. Phys.* **124**, 184109 (2006).
- K. J. Bowers *et al.*, in *Proceedings of the 2006 Association for Computing Machinery/Institute of Electrical and Electronics Engineers (ACM/IEEE) Conference on Supercomputing (SC06)*, Tampa, FL, 11 to 17 November 2006 (ACM Press, New York, 2006).
- Single-letter abbreviations for the amino acid residues: A, Ala; C, Cys; D, Asp; E, Glu; F, Phe; G, Gly; H, His; I, Ile; K, Lys; L, Leu; M, Met; N, Asn; P, Pro; Q, Gln; R, Arg; S, Ser; T, Thr; V, Val; W, Trp; and Y, Tyr.
- H. Inoue, T. Noumi, T. Tsuchiya, H. Kanazawa, *FEBS Lett.* **363**, 264 (1995).
- O. Jardetzky, *Nature* **211**, 969 (1966).
- K. Nozaki, K. Inaba, T. Kuroda, M. Tsuda, T. Tsuchiya, *Biochem. Biophys. Res. Commun.* **222**, 774 (1996).
- A. L. Hodgkin, R. D. Keynes, *J. Physiol.* **128**, 61 (1955).
- S. Berneche, B. Roux, *Nature* **414**, 73 (2001).
- E. Olkhova, E. Padan, H. Michel, *Biophys. J.* **92**, 3784 (2007).
- Y. Gerchman *et al.*, *Proc. Natl. Acad. Sci. U.S.A.* **90**, 1212 (1993).
- A. Rimon, Y. Gerchman, Y. Olami, S. Schuldiner, E. Padan, *J. Biol. Chem.* **270**, 26813 (1995).
- N. Gutman, S. Steiner-Mordoch, S. Schuldiner, *J. Biol. Chem.* **278**, 16082 (2003).
- R. Needleman *et al.*, *J. Biol. Chem.* **266**, 11478 (1991).
- E. Olkhova, C. Hunte, E. Screpanti, E. Padan, H. Michel, *Proc. Natl. Acad. Sci. U.S.A.* **103**, 2629 (2006).
- L. Galili, A. Rothman, L. Kozachkov, A. Rimon, E. Padan, *Biochemistry* **41**, 609 (2002).
- A. Rimon, Y. Gerchman, Z. Kariv, E. Padan, *J. Biol. Chem.* **273**, 26470 (1998).
- E. Padan, N. Maisler, D. Taglicht, R. Karpel, S. Schuldiner, *J. Biol. Chem.* **264**, 20297 (1989).
- D. Zuber *et al.*, *Biochim. Biophys. Acta* **1709**, 240 (2005).
- Materials and methods are available as supporting material on Science Online.
- W. Humphrey, A. Dalke, K. Schulten, *J. Mol. Graph.* **14**, 33 (1996).
- W. L. DeLano, *The PyMOL Molecular Graphics System* (DeLano Scientific, San Carlos, CA, 2002).
- The authors would like to thank members of the Padan laboratory for helpful discussions, experimental

assistance, and reagents; F. Sacerdoti for invaluable help with computational resources; and A. Weber for editorial assistance. This research was supported in part by a grant from the Israel Science Foundation to I.T.A. A version of Desmond, the software used to perform the simulations described in this article, will be released by the end of 2007. This version will be made available by D. E. Shaw Research for noncommercial research use and by Schrödinger LLC for commercial use. Before release, the current version of Desmond will be available from the authors upon request under conditions described in the

SOM. D. E. Shaw Research and Schrödinger have entered into a licensing agreement for the commercial distribution of Desmond by Schrödinger. D.E.S. has a beneficial ownership interest in D. E. Shaw Research, and R.O.D., M.P.E., J.L.K., I.K., Y.S., and D.E.S. have beneficial ownership interests in Schrödinger. Each of these authors may thus benefit financially from any resulting sales of Desmond. D.E.S. is a member of the Board of Directors of the American Association for the Advancement of Science (AAAS), the publisher of *Science*, and serves as treasurer of the AAAS.

Supporting Online Material

www.sciencemag.org/cgi/content/full/317/5839/799/DC1
Materials and Methods
SOM Text
Figs. S1 to S4
Tables S1 to S4
References
Detailed Statement of Software Availability

21 March 2007; accepted 28 June 2007
10.1126/science.1142824

Augmented Wnt Signaling in a Mammalian Model of Accelerated Aging

Hongjun Liu,¹ Maria M Fergusson,^{1*} Rogerio M. Castilho,^{2*} Jie Liu,¹ Liu Cao,¹ Jichun Chen,³ Daniela Malide,⁴ Ilsa I. Rovira,¹ Daniel Schimel,⁵ Calvin J. Kuo,⁶ J. Silvio Gutkind,² Paul M. Hwang,¹ Toreen Finkel^{1†}

The contribution of stem and progenitor cell dysfunction and depletion in normal aging remains incompletely understood. We explored this concept in the *Klotho* mouse model of accelerated aging. Analysis of various tissues and organs from young *Klotho* mice revealed a decrease in stem cell number and an increase in progenitor cell senescence. Because *klotho* is a secreted protein, we postulated that *klotho* might interact with other soluble mediators of stem cells. We found that *klotho* bound to various Wnt family members. In a cell culture model, the Wnt-*klotho* interaction resulted in the suppression of Wnt biological activity. Tissues and organs from *klotho*-deficient animals showed evidence of increased Wnt signaling, and ectopic expression of *klotho* antagonized the activity of endogenous and exogenous Wnt. Both in vitro and in vivo, continuous Wnt exposure triggered accelerated cellular senescence. Thus, *klotho* appears to be a secreted Wnt antagonist and Wnt proteins have an unexpected role in mammalian aging.

Resident and circulating stem and progenitor cells are critical for ongoing tissue maintenance and repair, and it is often postulated that stem and progenitor cell depletion or dysfunction might contribute to aging (1). We therefore examined stem cell dynamics in a genetic model of accelerated aging. Mice lacking *klotho* expression, henceforth termed *Klotho* mice, have a shortened life span and exhibit a number of early-onset age-related changes, including arteriosclerosis, decreased fertility, and skin atrophy (2). *Klotho* is a transmembrane protein with a large extracellular domain composed of two repeats (KL1 and KL2 domains) that share similarity to Family I glycosidases. In addition to being cell-associated, the extracellular portion of

klotho is secreted and can be detected in the circulation of animals and humans (3). It is generally believed that secreted *klotho* is the form most likely mediating the protein's longevity effects.

One alteration in *Klotho* animals is the early appearance of age-related changes in the skin. To assess whether these phenotypic changes were accompanied by alterations in stem cell number, we identified the number of long-term 5-bromo-2'-deoxyuridine (BrdU)-retaining cells in the skin of either wild-type or age-matched *Klotho* animals (4). These label-retaining cells (LRCs) are a convenient method to identify stem cells within their niche (5). At an age of 2.5 months, *Klotho* mice had significantly fewer LRCs than their wild-type littermates [wild type: 80 ± 5 LRCs (\pm SD) per set of three follicles versus *Klotho*: 35 ± 3 LRCs, $n = 30$, $P < 0.05$ paired t test]. Skin LRCs are confined to a specialized region of the follicle known as the bulge region, and the stem cells contained within this niche are enriched for CD34 expression (6). The bulge region in *Klotho* animals was consistently smaller with reduced CD34 expression (Fig. 1A). Hair follicle epidermal stem cells are also a source of transient amplifying (TA) cells induced by acute wounding (7). Consistent with a defect in the number of LRCs, epidermal wounding resulted in a diminished number of TA cells in

the *Klotho* animals (Fig. 1B) and a deficit in wound closure (Fig. 1C).

Age-matched wild-type and *Klotho* skin sections also exhibited differences in senescence-associated endogenous β -galactosidase (SA β -gal) activity (Fig. 1D). The observed SA β -gal staining occurred in the outermost epidermal layer including the acellular stratum corneum. The specificity and physiological significance of this staining is unclear. Examination of numerous random follicles revealed that the *Klotho* animals also had intense β -galactosidase staining within the follicles, especially within regions known to contain rapidly dividing progenitor cells (8). We observed little to no SA β -gal staining in the intra-follicular regions. Senescent cells often activate the DNA damage response (DDR) pathway, as evidenced by the development of nuclear foci of proteins such as phosphorylated histone (H2AX), ataxia telangiectasia mutated (ATM), and binding protein 1 (53BP1) (9). The DDR pathway was activated in multiple random *Klotho* follicles but not in age-matched wild-type mice (Fig. 1D).

Klotho animals also demonstrated increased SA β -gal staining in the small intestine, especially within intestinal crypts, an area enriched for stem and progenitor cells (Fig. 1E). Similar analysis of the testis in male animals also demonstrated evidence of increased progenitor cell senescence (fig. S1). In the bone marrow of *Klotho* mice, there was also a reduction in the population of cells bearing the cell surface phenotype of c-kit⁺ sca-1⁺ lineage negative that encompasses the hematopoietic stem cell (HSC) (Fig. 1F). This reduction of HSC in *Klotho* animals was accompanied by a marked increase in the percentage of stem cells that were actively dividing (*Klotho* HSCs: $28.4 \pm 3.7\%$ in G₁ versus wild-type HSCs: $10.2 \pm 1.1\%$ in G₁, $n = 3$ animal pairs per group, $P < 0.05$ paired t test) (Fig. 1G).

Given that stem cell biology is regulated by a number of secreted factors, we wondered whether there might be a functional interaction between *klotho* and one of these known stem cell regulators. In the course of our experiments, we noted that the subcellular distribution of *klotho* and Wnt proteins within transfected cells overlapped (fig. S2). Thus, we sought to determine whether *klotho* and Wnt3 could form a direct molecular complex. Epitope-tagged Wnt3 and myc-tagged *klotho* were readily detectable in transfected cell lysates (Fig. 2A). *Klotho* associated with immu-

¹Cardiology Branch, National Heart, Lung, and Blood Institute, NIH, Bethesda, MD 20892, USA. ²Oral and Pharyngeal Cancer Branch, National Institute of Dental and Craniofacial Research, NIH, Bethesda, MD 20892, USA. ³Hematology Branch, National Heart, Lung, and Blood Institute, NIH, Bethesda, MD 20892, USA. ⁴Light Microscopy Core Facility, National Heart, Lung, and Blood Institute, NIH, Bethesda, MD 20892, USA. ⁵Mouse Imaging Facility, NIH, Bethesda, MD 20892, USA. ⁶Division of Hematology, Stanford University School of Medicine, Stanford, CA 94305, USA.

*These authors contributed equally to this work.

†To whom correspondence should be addressed. E-mail: finkel@nih.gov